CANCER

Diabetic hyperglycemia promotes primary tumor progression through glycation-induced tumor extracellular matrix stiffening

Wenjun Wang[1]†, Lauren A. Hapach[1,2]†, Lauren Griggs[3], Kyra Smart[1], Yusheng Wu[1], Paul V. Taufalele[1], Matthew M. Rowe[1], Katherine M. Young[1], Madison E. Bates[1], Andrew C. Johnson[1], Nicholas J. Ferrell[4], Ambra Pozzi[5,6], Cynthia A. Reinhart-King[1,2]*

Diabetes mellitus is a complex metabolic disorder that is associated with an increased risk of breast cancer. Despite this correlation, the interplay between tumor progression and diabetes, particularly with regard to stiffening of the extracellular matrix, is still mechanistically unclear. Here, we established a murine model where hyperglycemia was induced before breast tumor development. Using the murine model, in vitro systems, and patient samples, we show that hyperglycemia increases tumor growth, extracellular matrix stiffness, glycation, and epithelial-mesenchymal transition of tumor cells. Upon inhibition of glycation or mechanotransduction in diabetic mice, these same metrics are reduced to levels comparable with nondiabetic tumors. Together, our study describes a novel biomechanical mechanism by which diabetic hyperglycemia promotes breast tumor progression via glycating the extracellular matrix. In addition, our work provides evidence that glycation inhibition is a potential adjuvant therapy for diabetic cancer patients due to the key role of matrix stiffening in both diseases.

INTRODUCTION

Diabetes mellitus is a common endocrine disorder characterized by hyperglycemia resulting from defects in insulin secretion and/or insulin resistance (*1*). Clinical studies show that diabetes is correlated with an increased risk of numerous types of cancers, including liver, colon, pancreatic, bladder, breast, and rectal cancer (*2*). More specifically, evidence suggests that patients with breast cancer with a history of diabetes of greater than 5 years have a higher mortality rate than nondiabetic patients (*3*–*6*). Previous studies suggest that the diabetic state promotes tumor progression through several mechanisms, including hyperinsulinemia, hyperglycemia, and chronic inflammation (*3*). However, the role of changes to the extracellular matrix (ECM) caused by the diabetic milieu in cancer progression has been understudied.

Reducing sugars, such as glucose, can cause increased cross-linking and ECM modification in collagenous tissues via glycation (*7*–*9*). Glycation, as a nonenzymatic reaction of sugars with the amino groups of proteins, lipids, and nucleic acids, results in cross-linking and formation of advanced glycation end products (AGEs) (*9*). Glycation can interfere with normal protein function by disrupting conformation, altering enzymatic activity, and interfering with the ligand-receptor interaction (*10*, *11*). These protein-level disruptions can alter cell signaling and potentially influence tumor progression (*5*). In addition to altering cell signaling, hyperglycemia-induced glycation has also been shown to cross-link and stiffen collagen matrix in vitro (*7*, *12*, *13*). Since stiffening of the tumor ECM is known to promote malignancy (*14*, *15*), and sugars can promote matrix stiffening through glycation, we hypothesized that the diabetic state promotes tumor progression through nonenzymatic glycation-induced ECM stiffening.

Here, we show that hyperglycemia stiffens tumor ECM, promotes breast tumor progression, increases cell proliferation, and shifts tumor cells further along epithelial-to-mesenchymal transition (EMT). Notably, pharmaceutical inhibition of glycation or cell mechanical sensing in diabetic mice reduces tumor progression comparable to nondiabetic mice, while blood glucose levels are unaffected. Our results demonstrate a novel mechanism by which diabetes promotes breast tumor progression through glycation and point toward therapeutics targeting glycation as one mechanism to slow tumor growth in diabetics.

RESULTS

Diabetic hyperglycemia was established in FVB/N-Tg(MMTV-PyMT)634Mul/J mouse model

FVB/N-Tg(MMTV-PyMT)634Mul/J (PyMT) mice that develop spontaneous mammary tumors starting at 6 weeks after birth were used in this study. To induce hyperglycemia in PyMT mice, we fed the mice a high-fat diet starting at 4 weeks of age and then injected them with five daily consecutive 70 mg/kg doses of streptozotocin (STZ) at 5 weeks of age (Fig. 1A). While STZ-induced diabetes is a commonly used model, STZ can be carcinogenic and has been shown to induce lung, kidney, and uterine tumors in mice and kidney, pancreatic, and liver tumors in rats at high doses via generating DNA and chromosome damage (*16*–*18*). Thus, we next tested whether our STZ treatment influenced breast tumor progression independent of induction of hyperglycemia. MET-1 cells extracted from PyMT mice were treated with STZ for 5 days to mimic the STZ treatment performed on the mice in this study. DNA damage was quantified using a comet assay (*19*, *20*). No significant difference

[1]Department of Biomedical Engineering, Vanderbilt University, Nashville, TN 37235, USA. [2]Nancy E. and Peter C. Meinig School of Biomedical Engineering, Cornell University, Ithaca, NY 14853, USA. [3]College of Engineering, Pennsylvania State University, State College, PA 16802, USA. [4]Department of Internal Medicine, Division of Nephrology, Ohio State University Wexner Medical Center, Columbus, OH 43210, USA. [5]Division of Nephrology, Department of Medicine, Vanderbilt University School of Medicine, Nashville, TN 37232, USA. [6]Veterans Affairs Hospitals, Nashville, TN 37684, USA.
*Corresponding author. Email: cynthia.reinhart-king@vanderbilt.edu
†These authors contributed equally to this work.

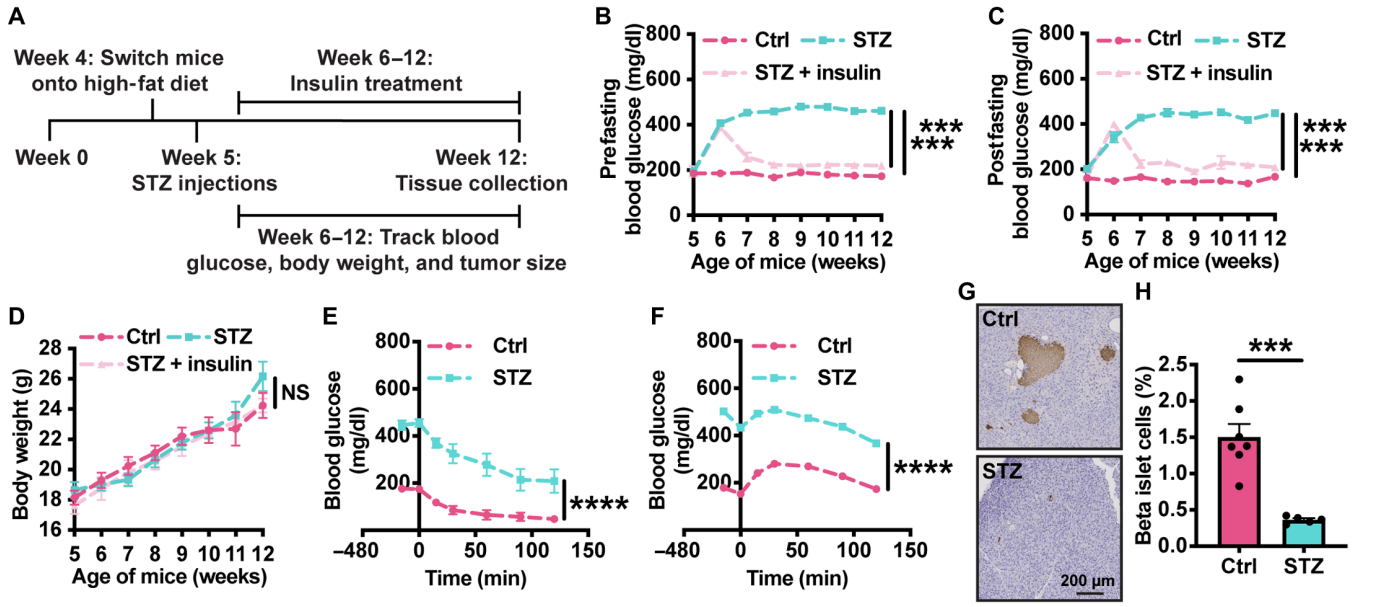

Fig. 1. Induction of diabetes mellitus within MMTV-PyMT mice. (**A**) Schematic overview of the diabetic MMTV-PyMT mouse model. (**B**) Prefasting and (**C**) postfasting blood glucose levels of MMTV-PyMT mice injected once daily with five consecutive daily 70 mg/kg doses of either STZ or sodium citrate buffer vehicle control (Ctrl) or treated with both STZ and insulin (STZ + insulin). (**D**) Body weight tracking of MMTV-PyMT mice injected once with five consecutive daily 70 mg/kg doses of either sodium citrate (Ctrl) or STZ or double-treated with both STZ and insulin (STZ + insulin). (**E**) Glucose levels over time after insulin injection for Ctrl group and STZ group. (**F**) Glucose levels over time postglucose injection for Ctrl group and STZ group during glucose tolerance assay. (**G**) Representative images of immunohistochemical staining for insulin in the pancreases of MMTV-PyMT mice injected with either sodium citrate (Ctrl) or STZ. (**H**) Quantification of beta islet cell percentage in the control group or mice injected with STZ (Ctrl, $N = 7$; STZ, $N = 5$; STZ + insulin, $N = 3$). Data are presented as means ± SEM. ***$P < 0.001$ and ****$P < 0.0001$. NS, not significant.

was observed in the DNA damage of cells with or without STZ treatment (fig. S2A). Since necrotic and apoptotic cells contain a large amount of damaged DNA and strand breaks, to ensure accuracy of the comet assay, cell death of control and STZ-treated cells was compared using a terminal deoxynucleotidyl transferase–mediated deoxyuridine triphosphate nick end labeling (TUNEL) assay. STZ treatment did not induce a significant change in cell death (fig. S2B). In addition, as a control, a group of STZ-treated mice was given insulin treatment using osmotic pumps to lower their blood glucose to a normal range. To verify the induction of hyperglycemia, blood glucose levels were measured weekly before and after fasting. At 12 weeks of age, the mice were euthanized, and tissue specimens were collected and analyzed. Compared with nondiabetic PyMT mice, blood glucose levels were significantly increased in the PyMT mice injected with STZ, while the insulin treatment decreased the blood glucose of STZ-treated mice to a comparable level with the nondiabetic group (Fig. 1, B and C). The blood glucose of STZ-injected mice increased to above 400 mg/dl and remained stably elevated over the entire course of the study. Body weight of control, STZ-injected, and STZ + insulin–treated mice increased steadily (Fig. 1D). Glucose and insulin tolerance tests performed at week 6 indicated that glucose levels of STZ-injected mice were increased compared with control group mice (Fig. 1, E and F). Staining of the pancreas of diabetic mice with anti-insulin antibody revealed a significant depletion of beta islet cells, the major cells targeted by STZ (Fig. 1, G and H). Together, these results showed that diabetic hyperglycemia was induced in MMTV-PyMT mice successfully at week 6 and could be reversed using an insulin pump.

Diabetic milieus causes stiffened tumor ECM through glycation

Since hyperglycemia results in increased glycation of ECM (*12*, *13*), we measured the level of glycated tumor ECM by immunohistochemistry (IHC) and Western blotting of AGEs. Tumors from diabetic mice showed increased AGEs compared to those from nondiabetic mice, while insulin treatment of diabetic mice significantly decreased tumor AGEs to levels comparable with nondiabetic mice (Fig. 2, A to D). Since sugars cross-link collagen through a nonenzymatic reaction resulting in stiffened matrix (*7*), we extended our investigation to assess collagen concentration, a major ECM component in mammary tumors, between diabetic and nondiabetic PyMT tumors. Tumor sections were stained with picrosirius red and imaged using quantitative polarization microscopy. There was no significant difference in optical retardance of the collagen signal observed between diabetic and nondiabetic tumors, indicating that collagen concentrations are similar between experimental groups (Fig. 2E). To assess whether hyperglycemia and the associated formation of AGEs stiffen the tumor ECM, we performed unconfined compression testing to examine the equilibrium modulus of diabetic and nondiabetic tumors. Tumors collected from diabetic mice had a higher equilibrium modulus compared with that from nondiabetic mice (Fig. 2F). Consistent with this result, atomic force microscopy (AFM) measurements indicated that hyperglycemia increased tumor elastic modulus compared to control mice, and insulin treatment of diabetic mice significantly decreased tumor elastic modulus to values comparable with control mice (Fig. 2, G to I). These data suggest that hyperglycemia-induced glycation stiffens

breast tumors (Fig. 2G) and increases the heterogeneity of tumor stiffness (Fig. 2, H and I).

Hyperglycemia promotes tumor progression in PyMT mice

Since hyperglycemia-induced glycation increases PyMT tumor stiffness, and ECM stiffness is known to promote tumor malignancy (*21*, *22*), we next investigated the progression of murine mammary tumors as a function of the diabetic state. Tumor volume of nondiabetic, diabetic, or diabetic mice treated with insulin was measured weekly until 12 weeks of age. Diabetic mice displayed accelerated tumor growth (Fig. 3A) and ultimately generated larger tumors (Fig. 3, B and C) compared with the nondiabetic group. Meanwhile,

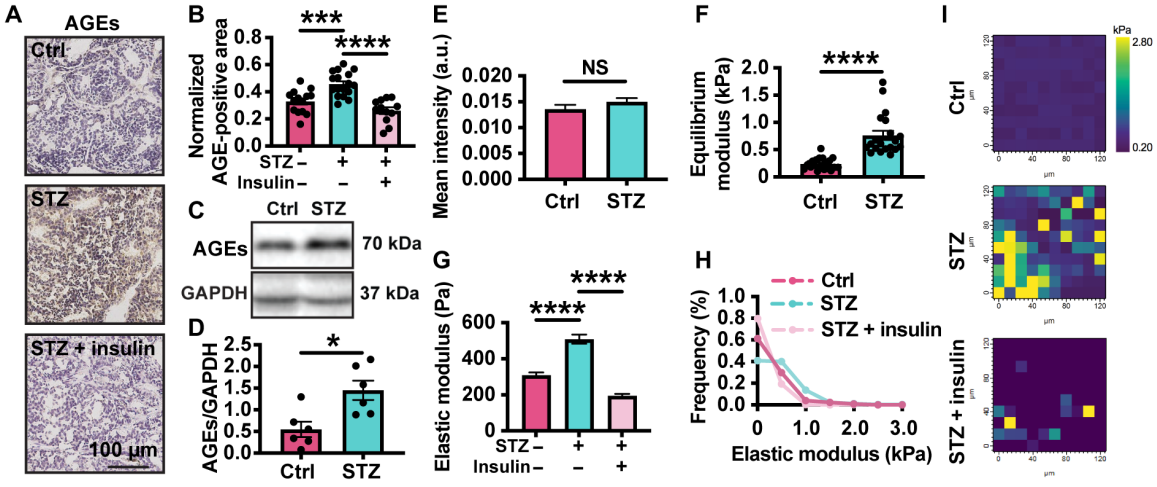

Fig. 2. Hyperglycemia promotes glycation and increases ECM stiffness. (**A**) Representative images of tumor sections with IHC staining for AGEs collected from nondiabetic (Ctrl), diabetic (STZ), and diabetic mice treated with insulin (STZ + insulin). (**B**) Corresponding quantification of normalized AGE-positive area (Ctrl, $N = 5$ and $n = 14$; STZ, $N = 4$ and $n = 17$; STZ + insulin, $N = 3$ and $n = 12$). (**C**) Representative Western blot protein bands for AGEs and GAPDH in tumors from diabetic (STZ) and nondiabetic (Ctrl) mice. (**D**) Corresponding quantification of AGEs normalized by GAPDH ($N = 4$ and $n = 6$). (**E**) Quantification of collagen deposition of diabetic and nondiabetic tumors ($N = 3$ and $n = 3$; 30 measurements per condition). (**F**) Unconfined compression assay showing equilibrium modulus of tumors extracted from diabetic or nondiabetic mice (Ctrl, $N = 4$ and $n = 6$; STZ, $N = 4$ and $n = 5$; 20 measurements per condition). (**G**) Elastic modulus of nondiabetic (Ctrl), diabetic (STZ), and diabetic tumors treated with insulin (STZ + insulin) measured by AFM ($N = 3$ and $n = 3$; 250 to 300 measurement per condition). (**H**) Corresponding histogram of AFM measurements for nondiabetic (Ctrl), diabetic (STZ), and diabetic tumors treated with insulin (STZ + insulin). (**I**) Representative force map of tumors extracted from nondiabetic (Ctrl), diabetic (STZ), and diabetic mice treated with insulin (STZ + insulin). Data are presented as means ± SEM. *$P < 0.05$, ***$P < 0.001$, and ****$P < 0.0001$. a.u., arbitrary units.

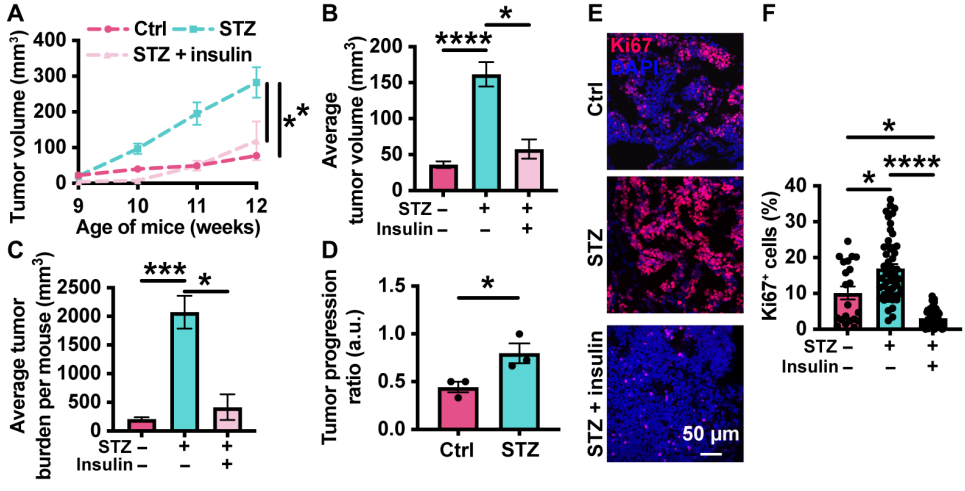

Fig. 3. Hyperglycemia increases tumor growth through promoting cell proliferation. (**A**) Weekly average tumor volume measurements for nondiabetic (Ctrl), diabetic (STZ), and diabetic mice treated with insulin (STZ + insulin) from when tumors become palpable and large enough for caliper measurements (week 9) to study endpoint (Ctrl, $N = 14$; STZ, $N = 12$; STZ + insulin, $N = 3$). (**B**) Average tumor volume for control (Ctrl), diabetic (STZ), and diabetic mice treated with insulin (STZ + insulin) at study endpoint (Ctrl, $N = 7$ and $n = 22$; STZ, $N = 13$ and $n = 75$; STZ + insulin, $N = 3$ and $n = 12$). (**C**) Average tumor burden per mouse for control (Ctrl), diabetic (STZ), and diabetic mice treated with insulin (STZ + insulin) at study endpoint (Ctrl, $N = 7$; STZ, $N = 22$; STZ + insulin, $N = 3$). (**D**) Tumor differentiation grading of tumors extracted from control group and mice treated with STZ ($N = 3$ and $n = 3$). (**E**) Representative images showing Ki67 and nucleus colocalization within nondiabetic, diabetic (STZ), and diabetic tumors treated with insulin (STZ + insulin). (**F**) Corresponding quantification of the percentage of cells with Ki67$^+$ nuclei (Ctrl, $N = 7 = 3$ and $n = 3$, 21 imaging fields; STZ, $N = 4$ and $n = 6$, 67 imaging fields; STZ + insulin, $N = 3$ and $n = 8$, 80 imaging fields included). Data are presented as means ± SEM. *$P < 0.05$, ***$P < 0.001$, and ****$P < 0.0001$. DAPI, 4′,6-diamidino-2-phenylindole.

insulin treatment significantly slowed down the tumor growth of diabetic mice. Histological analysis revealed that diabetic tumors are less differentiated and more malignant compared with nondiabetic tumors (Fig. 3D). To determine whether increased tumor cell proliferation was responsible for the increased tumor growth observed in diabetic mice, we quantified the percentage of cells with $Ki67^+$ nuclei using immunofluorescence staining (Fig. 3E). The results indicated that cell proliferation was significantly promoted by hyperglycemia status and inhibited when lowering the blood glucose via insulin treatment (Fig. 3F).

Hyperglycemia shifts PyMT tumors toward EMT phenotype

Matrix stiffening promotes tumor cell EMT (*23*), which is associated with increased tumor aggressiveness and worsened patient prognosis. Thus, we next investigated whether hyperglycemia-induced glycation affects tumor progression through up-regulation of EMT. Analysis of epithelial (E-cadherin) and mesenchymal (vimentin) markers (Fig. 4A) revealed that the ratio of vimentin expression to E-cadherin expression is greater in diabetic tumors compared to control ones (Fig. 4B). Further, this ratio is lowered to levels comparable with control tumors in diabetic tumors with insulin treatment. Together, this indicates that diabetic hyperglycemia is causing a shift toward EMT. Since increased expression of fibronectin has been associated with the prometastatic breast cancer phenotype and is known to induce changes in cell morphology and expression of EMT markers (*24*), fibronectin expression of tumors from nondiabetic, diabetic, and diabetic tumors was analyzed by IHC staining. Tumors of diabetic mice have more fibronectin than those of nondiabetic mice (Fig. 4, C and D). Decreasing blood glucose levels of diabetic mice via insulin treatment significantly lowered the amount of fibronectin in diabetic tumors. In addition to fibronectin, tumors from diabetic mice have more tumor growth factor–β (TGF-β) compared with nondiabetic tumors (Fig. 4, E to I). As TGF-β is a key player in regulating EMT, our results suggest that diabetic tumors are shifted further along the EMT spectrum toward an aggressive mesenchymal phenotype compared to nondiabetic tumors and that insulin treatment prevents this shift.

Glycation inhibition lowers ECM stiffness

Noting that glycation is a multistep, chemical reaction that increases ECM stiffness, we tested whether glycation inhibition via aminoguanidine (AG) or AGE cross-link breaker, alagebrium (ALT711), could ameliorate the observed phenotypes in diabetic mice (Fig. 5A) (*8*). The blood glucose of mice was measured weekly to verify that the glycation inhibitors did not affect blood glucose throughout the experiment (Fig. 5B). To determine whether glycation inhibition affected AGE concentration in STZ-injected mice, IHC staining was performed. AGE concentration was decreased in STZ-injected mice that received either inhibitor treatment compared to STZ-injected diabetic control mice (Fig. 5, C and D). When collagen concentration was assessed, no significant difference in mean optical retardance between STZ-injected mice treated or not with the inhibitors was observed (Fig. 5E). Bulk mechanical stiffness was assessed using unconfined compression testing. Both AG and ALT711 treatments lowered STZ-injected mouse tumor stiffness to that of control nondiabetic mouse tumors (Fig. 5F). To compare microscale stiffness, AFM measurements were performed on tumor samples with and without glycation inhibition. The average elastic modulus for tumors from diabetic mice treated with either inhibitor was

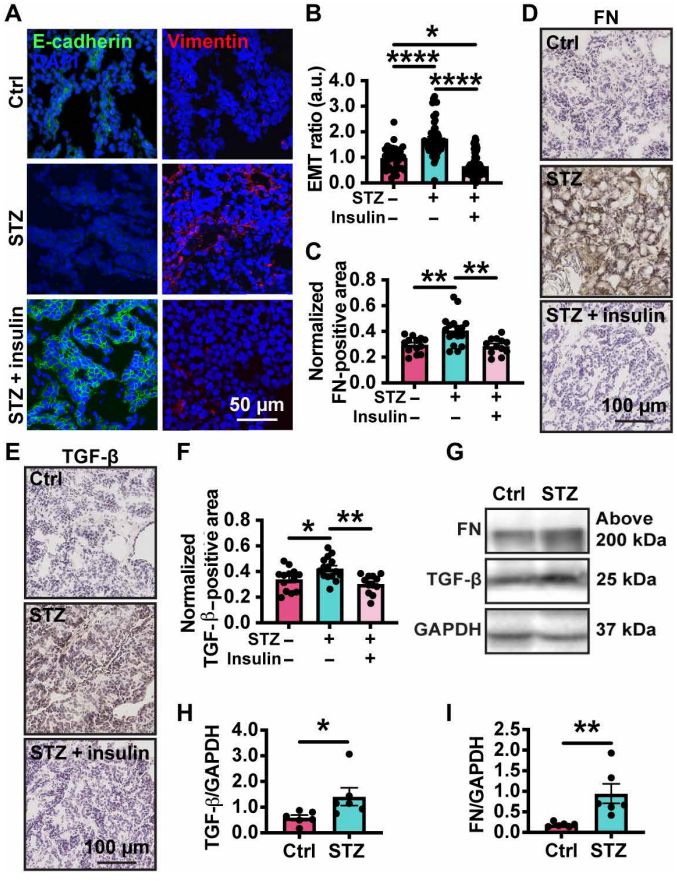

Fig. 4. Diabetes promotes EMT. (**A**) Representative images of immunofluorescence staining showing E-cadherin and vimentin of tumors extracted from nondiabetic (STZ), diabetic (STZ), and diabetic tumors treated with insulin (STZ + insulin). (**B**) Corresponding expression ratio of E-cadherin and vimentin (Ctrl and STZ, $N = 3$ and $n = 5$, 37 fields per tumor section; STZ + insulin, $N = 3$ and $n = 8$; 80 fields per tumor section were imaged). (**C**) Representative images showing fibronectin (FN) expression within tumors extracted from nondiabetic (Ctrl), and diabetic tumors treated with (STZ + STZ) or without (STZ) insulin. (**D**) Corresponding quantification of fibronectin-positive area within tumors (Ctrl, $N = 4$ and $n = 13$; STZ, $N = 5$ and $n = 17$; STZ + insulin, $N = 3$ and $n = 12$). (**E**) Representative images of TGF-β–stained tumor sections extracted from control (Ctrl) or diabetic mice treated with (STZ + insulin) or without (STZ) insulin. (**F**) Corresponding quantification of TGF-β–positive area within tumors (Ctrl, $N = 3$ and $n = 13$; STZ, $N = 5$ and $n = 15$; STZ + insulin, $N = 3$ and $n = 12$). (**G**) Protein bands generated by Western blotting showing fibronectin and TGF-β expression within diabetic (STZ) and nondiabetic (Ctrl) tumors. GAPDH was used as the loading control. (**H** and **I**) Corresponding quantification of fibronectin (H) and TGF-β (I) expression normalized over GAPDH expression ($N = 3$ and $n = 6$). Data are presented as means ± SEM. $^*P < 0.05$, $^{**}P < 0.01$, and $^{****}P < 0.0001$.

decreased compared to those from diabetic control mice (STZ only) (Fig. 5G). The distribution of elastic modulus values shows an overall shift toward lower values along with an absence of upper range values in AG- or ALT711-treated diabetic tumors compared to untreated diabetic controls (Fig. 5H). These experiments suggest that the increased stiffness in tumors from diabetic mice is due to increased glycation, which is successfully abrogated to nondiabetic control tumor levels by either AG or ALT711 AGE-inhibiting treatment, resulting in lower tumor ECM stiffness despite mice still presenting with hyperglycemia.

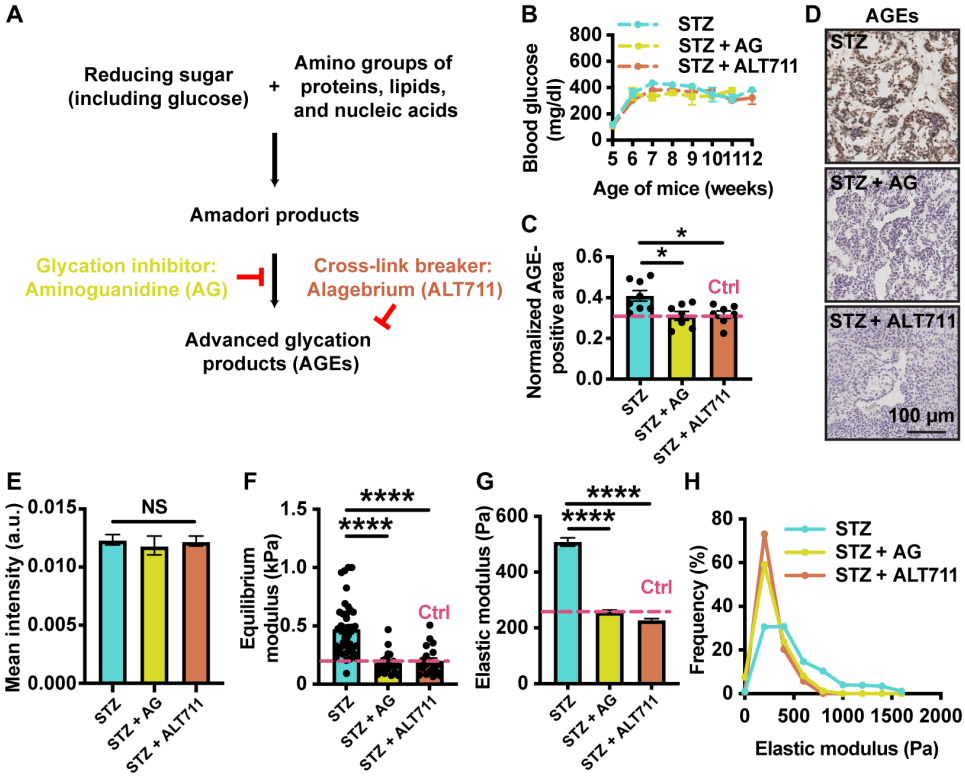

Fig. 5. Glycation inhibition decreases ECM stiffness. (**A**) Schematic overview of glycation reaction showing how glycation inhibitors block this reaction. (**B**) Blood glucose of diabetic mice treated with or without glycation inhibitors (STZ, $N = 12$; STZ + AG, $N = 10$; STZ + ALT711, $N = 12$). (**C**) Corresponding quantification of normalized AGE-positive area (STZ, $N = 4$ and $n = 8$; STZ + AG, $N = 3$ and $n = 7$; STZ + ALT711, $N = 4$ and $n = 7$). (**D**) Representative images of tumor sections with IHC staining for AGEs collected from diabetic mice treated with AG or ALT711. (**E**) Quantification of collagen deposition of diabetic and nondiabetic tumors (STZ, $N = 5$ and $n = 7$; 349 measurements per condition; STZ + AG, $N = 2$ and $n = 5$; 126 measurements per condition; STZ + ALT711, $N = 4$ and $n = 8$; 284 measurements per condition). (**F**) Unconfined compression assay showing equilibrium modulus of tumors extracted from diabetic mice treated with glycation inhibitors, AG or ALT711 (STZ, $N = 6$ and $n = 6$, 40 measurements included; STZ + AG, $N = 5$ and $n = 7$, 20 measurements included; STZ + ALT711, $N = 3$ and $n = 6$, 20 measurements included). (**G**) Elastic modulus of diabetic tumors treated with or without glycation inhibitors measured by AFM ($N = 3$ and $n = 3$, 430 to 589 measurements per condition). (**H**) Corresponding histogram of AFM measurements of diabetic tumors treated with or without glycation inhibitors. Data are presented as means ± SEM. *$P < 0.05$ and ****$P < 0.0001$.

Glycation promotes progression of primary tumors via increasing ECM stiffness

As ECM stiffness is known to promote malignancy (*21*, *22*), and glycation inhibition via AG or ALT711 treatment decreased ECM stiffness in STZ-injected mice, we assessed whether glycation inhibition also altered tumor progression via increased ECM stiffness. Tumor volume over time for the diabetic mice with either AG or ALT711 treatment was significantly lower than the volume of diabetic STZ only control tumors (Fig. 6A). At the study endpoint, the average tumor volume was significantly lower for STZ-injected mice with either inhibitor treatment compared to STZ only control mice (Fig. 6B). In addition, the average total tumor burden per mouse was significantly lower for glycation inhibitor–treated diabetic mice compared to diabetic-only controls (Fig. 6C). Significantly fewer Ki67-positive cells were detected in glycation-inhibited diabetic tumors than diabetic control tumors (Fig. 6, D and E). These data suggest that inhibition of glycation decreases the development of primary tumors and inhibits cell proliferation.

To confirm that the effect of glycation inhibitors on tumor progression inhibition is not due to potential side effects on the tumor cells rather than the ECM, MET-1 cells, which are mammary tumor cells isolated from MMTV-PyMT mice, were treated with AG or ALT711 at different concentrations for 72 hours. Proliferation of these cells was compared by quantifying the percentage of cells with $Ki67^+$ nuclei. Neither AG nor ALT711 treatment disrupted cell proliferation significantly (fig. S2, C and D). We also verified that different treatment times have no significant influence on cell proliferation by comparing $Ki67^+$ nuclei density of cells treated with either AG or ALT711 for 24 or 72 hours at 1000 mM concentration (fig. S2E). Noting that glycation can also activate AGEs and their receptor (AGE-RAGE) signaling in addition to stiffening the matrix (*7*, *12*, *13*), we also evaluated the cell proliferation of MET-1 cells with normal or decreased RAGE expression seeded on compliant or stiff matrix. Quantification of the density of cells with $Ki67^+$ nuclei indicated that while inhibition of RAGE expression using short hairpin RNA (shRNA; Santa Cruz, sc-36375-SH) decreased cell proliferation significantly, cell proliferation increased with increasing matrix stiffness (Fig. 6F). A similar effect was observed in cells embedded in a three-dimensional compliant or stiff collagen matrix, where stiffness was controlled through glycation with different amounts of glucose (Fig. 6G). These data suggest that glycation-mediated matrix stiffening promotes cell proliferation regardless of activation of AGE-RAGE interactions. Analysis of EMT markers showed that the EMT ratio was lower for glycation inhibitor-treated STZ tumors

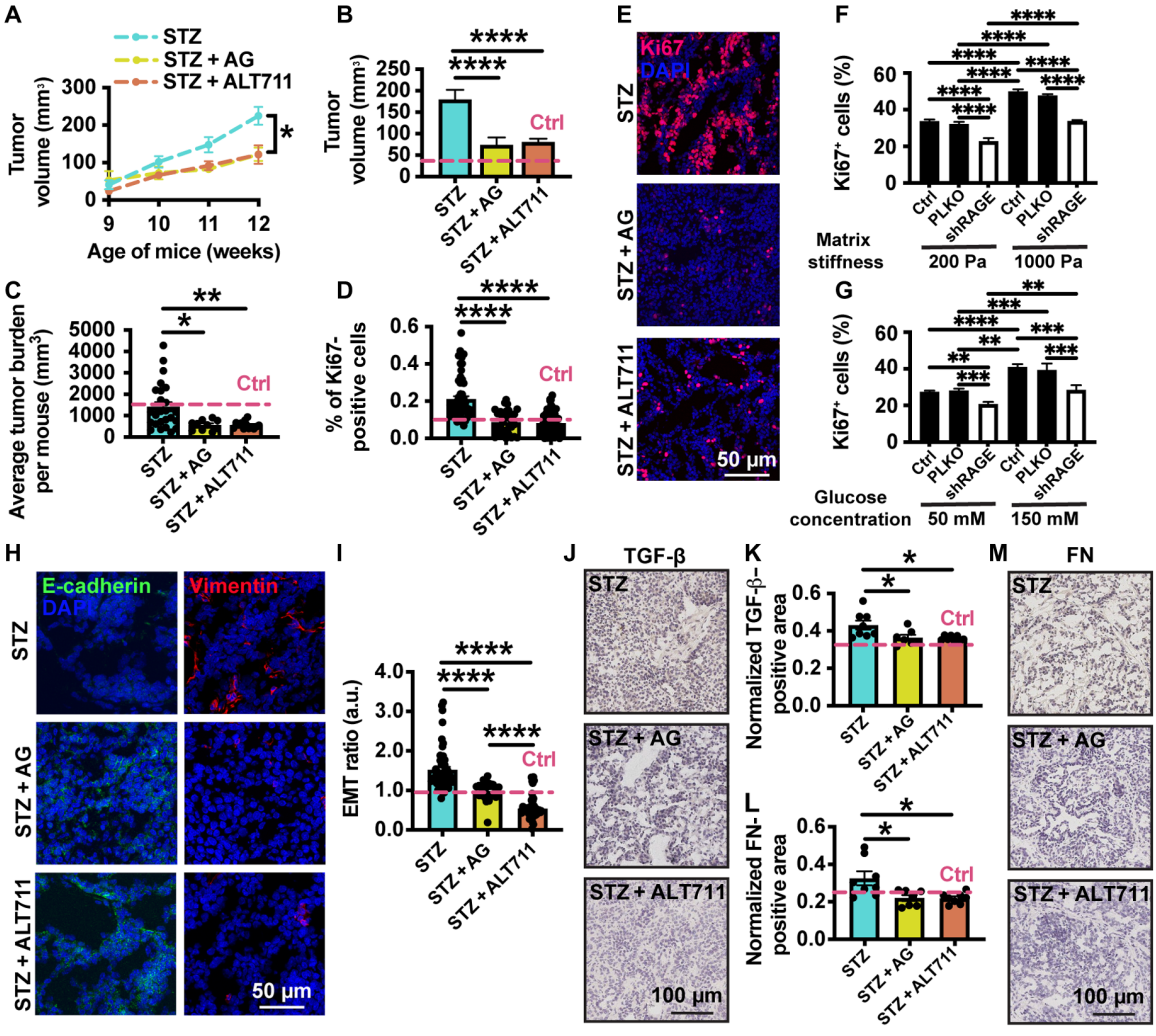

Fig. 6. Glycation inhibition decreases primary tumor progression. (**A**) Weekly tumor volume measurements for diabetic mice treated with AG or ALT711 from week 9 to study endpoint ($N = 6$ to 12). (**B**) Average tumor volume at study endpoint ($N = 6$ to 12). (**C**) Average tumor burden per mouse at study endpoint ($N = 9$ to 18). (**D**) Quantification of percentage of cells with Ki67$^+$ nuclei ($N = 3$ to 5 and $n = 3$ to 8, 32 to 64 imaging fields). (**E**) Representative images showing cells with Ki67$^+$ nuclei. (**F**) Comparison of proliferation of MET-1 cells with normal or decreased RAGE expression on substrates with 200- or 1000-Pa stiffness ($N = 3$ and $n = 45$). PLKO, pLKO.1 vector. (**G**) Quantification of proliferation of MET-1 cells embedded in collagen matrix ($N = 3$ and $n = 45$). (**H**) Representative images showing E-cadherin and vimentin of tumors. (**I**) Corresponding quantification of E-cadherin and vimentin expression ratio ($N = 3$ to 5 and $n = 4$ to 7, 25 to 64 fields). (**J**) Representative images of TGF-β–stained tumor sections. (**K**) Corresponding quantification of TGF-β–positive area within tumors ($N = 3$ to 4 and $n = 7$ to 8). (**L**) Corresponding quantification of fibronectin-positive area ($N = 3$ to 4 and $n = 7$ to 8). (**M**) Representative images showing fibronectin within tumors. Data are presented as means ± SEM. *$P < 0.05$, **$P < 0.01$, ***$P < 0.001$, and ****$P < 0.0001$.

compared to STZ-treated controls (Fig. 6, H and I). Similarly, the levels of TGF-β– and fibronectin-positive areas were significantly reduced in diabetic tumors treated with the inhibitors (Fig. 6, J to M). These results indicated that glycation inhibition shifted the EMT spectrum of diabetic tumors toward an epithelial phenotype. Cumulatively, these results suggest that glycation inhibition by either AG or ALT711 treatment reduces tumor aggressiveness in mice with diabetic hyperglycemia.

Inhibition of FAK-mediated cell mechanical sensing slows down the progression of diabetic tumors without influencing ECM stiffness

To confirm that glycation promotes tumor progression via stiffening tumor ECM, which then activates cell mechanical sensing signaling, STZ-injected mice were treated with a focal adhesion kinase (FAK) inhibitor, PF573228, for 7 weeks until the study endpoint. PF573228 is a small-molecule inhibitor of phosphorylation of FAK at Tyr^{397} and is currently in preclinical trials (*25*). The inhibition efficiency of PF573228 was confirmed using immunofluorescence staining showing phosphorylated FAK concentration within diabetic tumors treated with or without FAK inhibitor (fig. S2F). Over time, tumor volume of the diabetic mice treated with FAK activation inhibitor (FAKi) was significantly lower than the volume of diabetic control tumors (Fig. 7A). At the study endpoint, the average tumor volume was significantly lower for STZ-injected mice with FAKi treatment compared to STZ only control mice (Fig. 7B). In addition, the average total tumor burden per mouse was significantly lower for FAKi-treated diabetic mice compared to diabetic only controls (Fig. 7C). Significantly

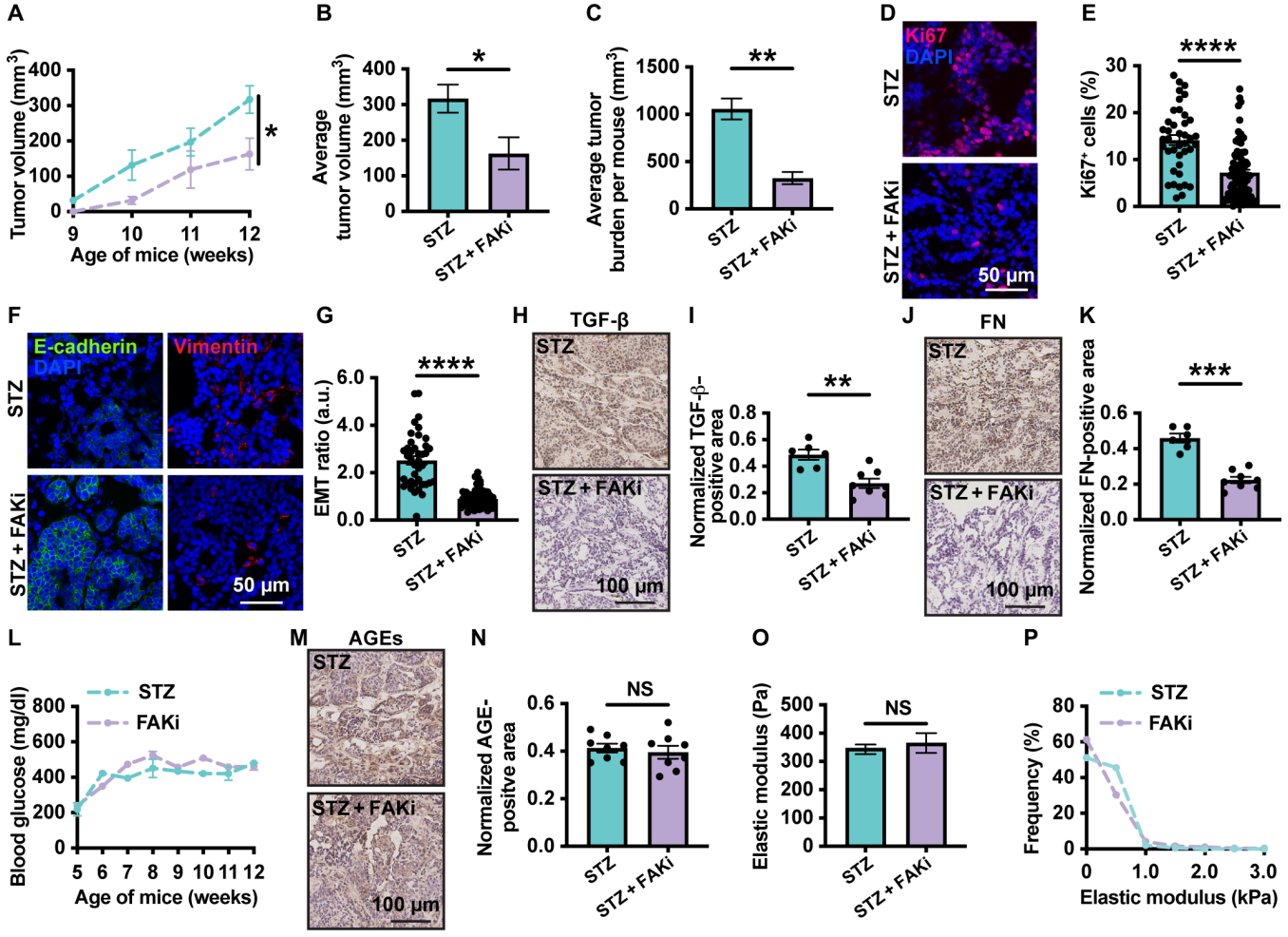

Fig. 7. FAK inhibition decreases tumor progression without influencing ECM stiffness. (**A**) Weekly tumor volume measurements for diabetic mice treated with or without FAK inhibitor ($N = 3$). (**B**) Average tumor volume at study endpoint ($N = 3$ and $n = 6$ to 10). (**C**) Average tumor burden per mouse at the study endpoint ($N = 3$). (**D**) Representative images showing Ki67 and nucleus colocalization within tumors. (**E**) Quantification of percentage of cells with Ki67$^+$ nuclei ($N = 3$ and $n = 8$, 40 to 80 imaging fields). (**F**) Representative images showing E-cadherin and vimentin of tumors. (**G**) Corresponding quantification of the expression ratio of E-cadherin and vimentin ($N = 3$ and $n = 8$, 40 to 80 imaging fields). (**H**) Representative images of TGF-β–stained tumor sections. (**I**) Corresponding quantification of TGF-β–positive area within tumors ($N = 3$ and $n = 6$ to 8). (**J**) Representative images showing fibronectin expression within tumors. (**K**) Corresponding quantification of fibronectin-positive area within tumors ($N = 3$ and $n = 6$ to 8). (**L**) Blood glucose of diabetic mice treated with or without FAKi ($N = 3$). (**M**) Representative images of tumor sections with IHC staining for AGEs. (**N**) Corresponding quantification of normalized AGE-positive area ($N = 3$ and $n = 8$). (**O**) Elastic modulus of diabetic tumors treated with or without FAKi ($N = 3$ and $n = 4$, 584 to 882 measurements). (**P**) Corresponding histogram of AFM measurements. Data are presented as means ± SEM. *$P < 0.05$, **$P < 0.01$, ***$P < 0.001$, and ****$P < 0.0001$.

fewer Ki67-positive cells were detected in FAK activation–inhibited diabetic tumors than in diabetic control tumors (Fig. 7, D and E). These data suggest that inhibition of cell mechanical sensing decreases the development of primary tumors and inhibits cell proliferation. Analysis of EMT markers indicated that the EMT ratio was lower for FAKi-treated STZ tumors compared to STZ-treated controls (Fig. 6, F and G). Similarly, the levels of TGF-β– and fibronectin-positive areas were significantly reduced in diabetic tumors treated with FAKi (Fig. 7, H to K). These results indicated that inhibition of FAK activation prevented the shift of diabetic tumors along the EMT spectrum toward a mesenchymal phenotype.

We also verified that FAK activation inhibition does not have an effect on the blood glucose, glycation, and ECM stiffness of tumors within diabetic mice. The blood glucose of mice was measured weekly to verify that the FAKi did not affect blood glucose throughout the experiment (Fig. 7L). To determine whether FAKi treatment affected AGE concentration in STZ-injected mice, IHC staining was performed. There was no significant difference in AGE concentration between STZ-injected mice that received inhibitor and STZ-injected diabetic control mice (Fig. 7, M and N). To compare the stiffness of tumor ECM, AFM measurements were performed on tumor samples with and without FAK activation inhibition. The average elastic modulus and the distribution of elastic modulus for tumors from diabetic mice treated with FAKi were similar to those from diabetic control mice (STZ only) (Fig. 7, O and P). These experiments suggest that inhibition of FAK activity does not influence the glycation reaction and stiffness of tumor ECM. Cumulatively, these results suggest that inhibition of cell mechanical sensing reduces tumor aggressiveness in mice with diabetic hyperglycemia without influencing stiffness of tumor ECM. These data suggest that cell mechanical

sensing is involved in the promotion of breast tumor progression by diabetic hyperglycemia-mediated glycation.

Diabetes activates glycation, increases ECM stiffness, promotes cell proliferation, and up-regulates EMT within tumor specimens from patients with breast cancer

Our in vivo data suggest that hyperglycemia-mediated glycation increases ECM stiffness and promotes breast tumor progression. To verify this finding clinically, AGE concentration within the stroma of diabetic and nondiabetic human breast tumors was quantified with IHC staining (Fig. 8, A and B), and matrix stiffness was measured with AFM (Fig. 8, C and D). Early-stage breast tumors (stage I/II) isolated from diabetic patients have higher AGE concentrations and increased ECM stiffness than those extracted from patients who were not diagnosed with diabetes. Moreover, consistent with our in vivo data, there were significantly more Ki67-positive cells in tumors extracted from diabetic patients compared to those from nondiabetic patients (Fig. 8, E and F). Consistent with this finding, the EMT ratio, the level of TGF-β, and fibronectin were significantly higher in tumors from diabetic patients (Fig. 8, G to L). Together, these data indicate that tumors in diabetic breast cancer patients have more glycation, increased ECM stiffness, increased cell proliferation, and up-regulated EMT, supporting our in vivo murine data indicating that diabetic hyperglycemia-mediated glycation promotes breast cancer progression via matrix stiffening.

DISCUSSION

Here, we show that diabetic hyperglycemia promotes breast tumor progression via glycation-mediated tumor ECM stiffening. Pharmacological inhibition of glycation was sufficient to decrease tumor progression of diabetic mice independently of the hyperglycemia status. We have established a novel mouse model where diabetic hyperglycemia is established in female MMTV-PyMT mice via STZ injections and high-fat diet before spontaneous mammary tumor generation. Using this model, we have uncovered and described a previously unknown role for nonenzymatic glycation in promoting tumorigenesis under hyperglycemic conditions. Compared to nondiabetic tumors, diabetic mouse tumors were stiffer, more proliferative, and further along the EMT spectrum, all of which correlate with worsened prognosis (*26*–*28*). Using AGE inhibitors, we mechanistically demonstrated that AGE-mediated cross-linking uniquely contributes to the enhanced tumorigenesis present in hyperglycemic mice. This murine model shows great potential in further probing the synergy between diabetes and cancer progression. Our findings highlight the importance of considering the interplay between diabetes and cancer, as both rank in the top 10 causes of death in the United States (*29*).

The effects of glycation and AGEs resulting from chronic hyperglycemia are far-reaching and have been implicated in numerous diabetes-associated complications including retinopathy, neuropathy, nephropathy, and cardiomyopathy (*30*). While other studies have focused on the chemical signaling role of RAGEs, RAGEs, in cancer

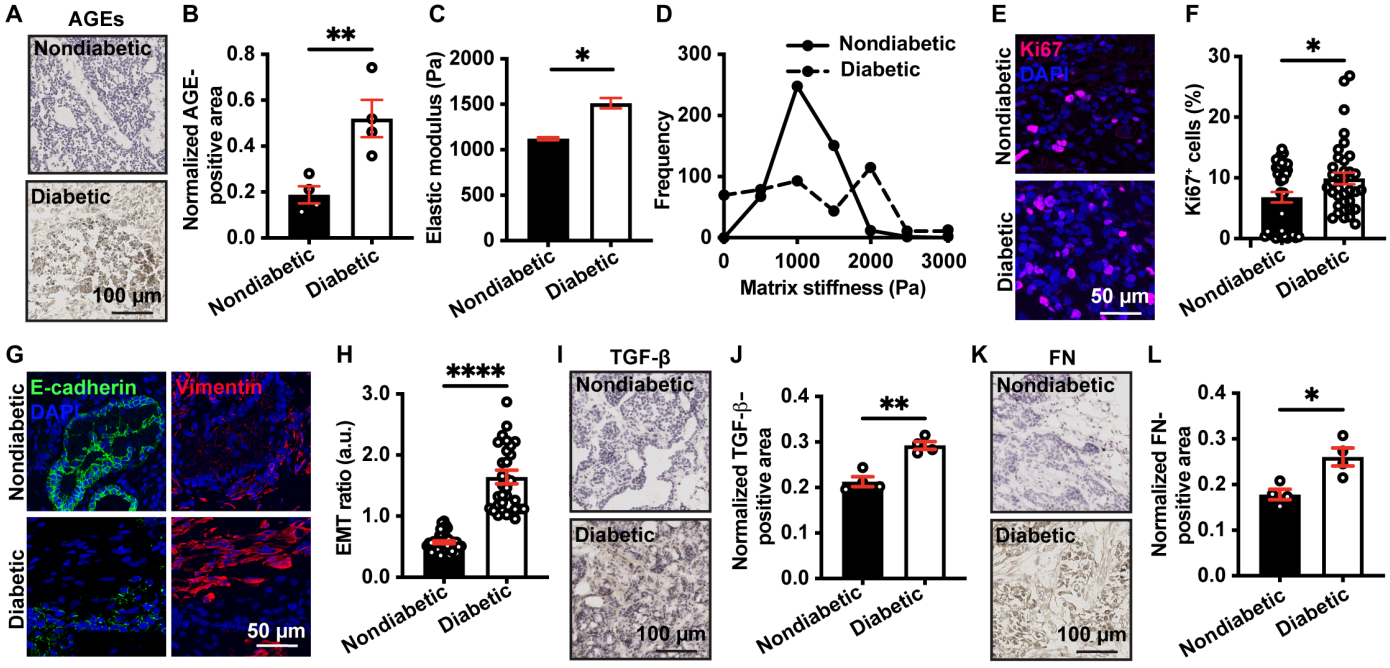

Fig. 8. Diabetes activates glycation, promotes cell proliferation, and shifts EMT within tumors from patients with breast cancer. (**A**) Representative images of tumor sections with IHC staining for AGEs within tumors extracted from patients with breast cancer diagnosed with or without diabetes. (**B**) Corresponding quantification of normalized AGE-positive area ($N = 4$). (**C**) Elastic modulus of tumors from diabetic or nondiabetic patients measured by AFM ($N = 4$, 478 to 482 measurements per condition). (**D**) Corresponding histogram of AFM measurements of diabetic or nondiabetic tumors. (**E**) Representative images showing Ki67 and nucleus colocalization within tumors extracted from patients with breast cancer diagnosed with or without diabetes. (**F**) Quantification of the percentage of cells with Ki67$^+$ nuclei ($N = 4$, 40 imaging fields included). (**G**) Representative images of immunofluorescence staining showing E-cadherin and vimentin of tumors extracted from diabetic or nondiabetic patients ($N = 4$, 40 imaging fields included). (**H**) Quantification of EMT ratio ($N = 4$, 40 imaging fields included). (**I**) Representative images of TGF-β–stained tumor sections extracted from diabetic and nondiabetic patients. (**J**) Corresponding quantification of TGF-β–positive area within tumors ($N = 4$). (**K**) Representative images showing fibronectin expression within tumors. (**L**) Corresponding quantification of fibronectin-positive area within tumors ($N = 4$). Data are presented as means ± SEM. *$P < 0.05$, **$P < 0.01$, and ****$P < 0.0001$.

progression, we also focus on the mechanical role of nonenzymatic glycation, where AGEs are a bioactive byproduct of this reaction (*31*, *32*). To parse apart the effect of the mechanical cross-linking and AGE signaling, we implemented treatment with two inhibitors, AG and alagebrium, which affect different steps in the nonenzymatic glycation reaction. As AG inhibits AGE formation, this inhibitor blocks both the chemical and mechanical effects of the nonenzymatic glycation (*33*). Alagebrium acts as an AGE cross-link breaker that allows AGEs to form but removes the cross-links, effectively permitting chemical signaling while negating the mechanical effects of nonenzymatic glycation (*34*). As we found similar effects across all metrics for both AG- and alagebrium-treated diabetic mice, our findings suggest that AGE-mediated ECM stiffening plays a critical role in the increased aggressiveness of mammary tumors in hyperglycemic mice that cannot be compensated for by AGE-RAGE signaling alone. An important consideration that we have not addressed in this work is whether the enhanced tumor cell proliferation we observe in hyperglycemic mice is primarily driven directly by increased ECM stiffness or by enhanced tumor growth pressure associated with increased confinement due to ECM stiffness, which has also been shown to induce protumorigenic cell signaling in vitro and in vivo (*35*, *36*). Further studies to parse apart the exact cell mechanosensing mechanism would facilitate the discovery of more targeted therapies to benefit patients with these highly prevalent comorbidities.

AGEs have been implicated in numerous pathologies, including diabetes, cancer, atherosclerosis, rheumatoid arthritis, bone fragility fracture, kidney failure, Alzheimer's disease, and premature aging (*37*, *38*). While efforts have been made to develop and test a variety of AGE-inhibiting drugs, clinical trials have produced mixed results (*38*, *39*). As our study along with ample experimental and clinical evidence shows that outcomes are worsened for breast cancer patients with preexisting diabetes, this subset of diabetic cancer patients may uniquely benefit from the addition of AGE-inhibiting treatment to the traditional therapeutic strategy (*40*). One commonly used drug, metformin, which lowers blood glucose and is a first-line agent in the treatment of type II diabetes, is also known to inhibit AGEs (*41*). Diabetic patients on metformin have a roughly one-third reduction in cancer incidence and mortality compared to patients on other antidiabetic drugs (*42*). Outside of diabetes, metformin has recently shown incredible promise as a complementary therapeutic alongside standard-of-care treatment (*42*). Given the results of our study and the benefits of metformin in both diabetes and cancer treatments, further work to delineate the synergy of breast cancer and diabetes and test the potential complementary effects of other AGE-inhibiting drugs should be pursued.

MATERIALS AND METHODS

Antibodies and reagents

Antibodies used for staining in Western blot and IHC experiments were as follows: anti-AGE antibody (ab23722, Abcam, Cambridge, UK), anti-fibronectin antibody (sc-9068 and sc-6953, Santa Cruz Biotechnology, Dallas, TX, USA), anti–TGF-β antibody (ab92486, Abcam), and anti–glyceraldehyde-3-phosphate dehydrogenase (GAPDH) antibody (Poly6314; BioLegend, San Diego, CA, USA). Primary and secondary antibodies used in immunofluorescence staining included anti-vimentin antibody (ab92547, Abcam), anti–polyoma virus medium T antigen antibody (PyMT; ab15085, Abcam), anti–E-cadherin antibody (7870, Santa Cruz Biotechnology), anti-Ki67 antibody (14-5698-82, Thermo Fisher Scientific, Waltham, MA, USA), anti-rat Alexa Fluor 647 goat antibody (A21247, Thermo Fisher Scientific), and anti-rabbit Alexa Fluor 568 donkey antibody (A10042, Thermo Fisher Scientific). All other reagents used here were purchased from Thermo Fisher Scientific.

MMTV-PyMT transgenic mouse studies

FVB/N-Tg(MMTV-PyVT)634Mul/J (MMTV-PyMT) mice were used in this study. All mice were maintained following a protocol approved by the Vanderbilt University Institutional Animal Care and Use Committee (protocol no. M1700029-01). Female MMTV-PyMT mice of the FVB strain background (The Jackson Laboratory, Bar Harbor, ME, USA) were fed with D12492 high-fat diet (NC0004611, Research Diet Inc., New Brunswck, NJ, USA) starting at 4 weeks of age. To induce diabetes, mice were given five consecutive daily doses of STZ (MilliporeSigma) through intraperitoneal injection at 70 mg/kg body weight. STZ is a small molecule that has been shown to selectively destroy pancreatic beta islet cells and induce diabetic hyperglycemia within mice (*43*). The control group of mice was injected with citrate buffer [0.1 mM (pH 4.5); MilliporeSigma] as vehicle control. Body mass, tumor volume, and glucose levels of mice were measured weekly starting before beginning STZ injections and continuing until the mice were euthanized. The tumor volume of the MMTV-PyMT transgenic mice was calculated as follows: $\pi \times \text{length}^2 \times \text{width}/12$ (*44*). Mice with a blood glucose level above 400 mg dl^{-1} were considered diabetic. To further determine that diabetes was induced in the mice, the presence of beta islet cells within the pancreas was quantified with IHC at the study endpoint.

For the STZ-treated mice receiving insulin, mice were treated with insulin glargine (MilliporeSigma) for 7 weeks via implantation of a subcutaneous insulin pump (ALZET mini osmotic pump, 0.5 U of insulin per mouse per day, Model 2006). The osmotic insulin pumps were implanted the day after diabetic hyperglycemia was confirmed (on week 6) (*45*). For STZ-injected mice receiving AG, mice were treated with 3 mg/kg body weight AG (MilliporeSigma) in drinking water until the study endpoint. For STZ-injected mice receiving alagebrium (ALT711) treatment, mice were treated with 1 mg/kg body weight alagebrium (MedChemExpress, Monmouth Junction, NJ, USA) injected daily intraperitoneally until study endpoint. For the STZ-treated mice receiving PF573229, 50 μM PF573228 (MedChemExpress) was injected subcutaneously daily until the endpoint of the study (*46*).

Seven weeks after STZ injection, mice were humanely euthanized by CO_2 asphyxiation and necropsied. Mammary tumors were collected and snap-frozen in 70% ethanol dry ice slurry or fixed with 4% (v/v) paraformaldehyde in phosphate-buffered saline (PBS). Snap-frozen samples were then sectioned at a thickness of 5 μm for immunofluorescence and immunohistochemical staining and at 20 μm for AFM. Fixed tissues were sectioned at a thickness of 5 μm for collagen quantification via picrosirius staining. Tumor aggressiveness was further assessed with hematoxylin and eosin staining followed by tumor grading by a blinded veterinary pathologist. Female mice have been found to be resistant to STZ-induced diabetic hyperglycemia (*47*). Noting this difficulty of inducing diabetic hyperglycemia in female mice, several other permutations of one of the commonly used methods, STZ injections, were also tested on our MMTV-PyMT mice (*43*, *48*, *49*). Our results showed that these

regimens of STZ injections either failed to elevate blood glucose at all (fig. S1, A to F) or elevated glucose at a delayed rate, so diabetic levels were not reached until week 8 when tumor progression had already initiated (fig. S1, G and H). (*50*).

Glucose and insulin tolerance assay

Glucose tolerance assay and insulin tolerance assay were also performed within 1 week after STZ injection. The mice were fasted 8 hours before both experiments. For glucose tolerance assay, mice were injected with sterile 10% glucose (MilliporeSigma) intraperitoneally at 1 g/kg body weight. For insulin tolerance assay, insulin (Eli Lilly, Indianapolis, IN, USA) was administered through intraperitoneal injection at 2 U/kg body weight. Blood was collected immediately before the administration and at 15, 30, 60, 90, and 120 min after administration.

Cell culture

MET-1 cells extracted from MMTV-PyMT mice were cultured in Dulbecco's modified Eagle's medium supplemented with 10% (v/v) fetal bovine serum (FBS) and 1% (v/v) penicillin-streptomycin (*20*). Cells were maintained at 37°C, humidified atmosphere of 5% (v/v) CO_2 in air. Cells were tested for mycoplasma contamination, and experiments were conducted under mycoplasma-negative conditions. For glycation inhibition studies, cells were seeded on collagen-coated coverslips and treated with either AG or ALT711 at 10, 100, or 1000 μM concentration for 24 or 72 hours. For cell proliferation assay, cells with normal or decreased RAGE expression were seeded onto collagen-coated polyacrylamide substrates or embedded in collagen matrix glycated with different amounts of glucose. For the comet assay and TUNEL assay, MET-1 cells were seeded on collagen-coated coverslips and treated with STZ (0.875 mg/ml) for 5 days. Cells were fixed with 3.7% (v/v) paraformaldehyde in PBS for 10 min at room temperature. Cells were kept in PBS at 4°C until downstream experiments.

Immunofluorescence

Tumor tissue sections extracted from MMTV-PyMT mice or MET-1 cells (+/− RAGE shRNA) receiving AG or ALT711 treatment were fixed with 4% (v/v) paraformaldehyde in PBS for 10 min at room temperature. After fixation, samples were washed with PBS and permeabilized with 1% (v/v) Triton X-100 (Thermo Fisher Scientific) in PBS. After permeabilization, tissue sections were then blocked with 10% (v/v) FBS, 5% (v/v) donkey serum, and 5% (v/v) goat serum for 2 hours at room temperature. Samples were then stained with primary antibodies, including anti-vimentin antibody (ab92547, Abcam), anti-PyMT antigen antibody (ab15085, Abcam), anti–E-cadherin antibody (7870, Santa Cruz Biotechnology), and anti-Ki67 antibody (14-5698-82, Thermo Fisher Scientific) at 1:50 diluted in PBS with 10% (v/v) FBS, 5% (v/v) donkey serum, and 5% (v/v) goat serum overnight at 4°C. After washing with PBS supplemented with 0.02% Tween 20, samples were then incubated with secondary antibodies, including goat anti-rat Alexa Fluor 647 antibody (A21247, Thermo Fisher Scientific) and donkey anti-rabbit Alexa Fluor 568 antibody (A10042, Thermo Fisher Scientific) at 1:100 diluted in PBS with 10% (v/v) FBS, 5% donkey serum, and 5% goat serum for 1 hour at room temperature in the dark. Immunofluorescent images were acquired with a Zeiss LSM800 confocal microscope using a 40×/1.1 numerical aperture (NA) water immersion objective and 405, 568, and 640 excitation laser lines and *z*-stack imaging. Protein colocalization analysis was performed as previously described (*51*). Briefly, filtered corresponding images were overlaid, and the overlap area was measured.

Western blot analysis

Snap-frozen tumors extracted from mice were ground using a precooled (−80°C) mortar and pestle. The pulverized tumor was then lysed in Laemmli buffer and centrifuged at 14,000*g* at 4°C for 10 min. The supernatant was collected and used for Western blotting. The protein concentration was measured with the DC Assay Kit (Bio-Rad), subjected to gel electrophoresis [8% (w/v) acrylamide gel], and transferred to polyvinylidene difluoride membranes as described previously (*52*). Membranes were then blocked with 5% bovine serum albumin (MilliporeSigma) in tris-buffered saline (TBS). Membranes were then incubated with primary antibody overnight at 4°C, washed with TBS supplemented with 0.1% Tween 20. After washing, membranes were stained with secondary antibody for 1 hour at room temperature. Primary antibodies were prepared at 1:1000 dilution in 5% bovine serum albumin. Secondary antibodies conjugated to horseradish peroxidase were prepared at 1:2000 dilution. Membranes were imaged with West Pico or West Dura (Thermo Fisher Scientific) per their respective protocols, using an ImageQuant LAS-4000 system. Quantification was performed with ImageJ [National Institutes of Health (NIH)].The relevant protein expression level was expressed as the ratio of the protein of interest to GAPDH.

Atomic force microscopy

ECM stiffness of tumors extracted from PyMT mice or patients with breast cancer was measured using contact mode AFM (MFP-3D, Asylum Research). Snap-frozen tissue samples were sectioned at a thickness of 20 μm and incubated in PBS supplemented with protease inhibitor cocktail (Thermo Fisher Scientific) during the measurement. A silicon nitride cantilever having a nominal spring constant of 0.06 N m^{-1} and 5-μm-diameter spherical borosilicate glass bead (Novascan, Boone, IA, USA) was used. The probe spring constant was measured before each session. Force-displacement curves were obtained by indenting two or three force maps (10-by-10 grid spaced 10 μm apart) on each tissue section with approach and retract speeds of 2 μm s^{-1} until reaching the maximum set force of 3 nN. To calculate elastic modulus from each indentation, the force-displacement curve was fitted to the Hertz model assuming a Poisson's ratio of 0.5.

Immunohistochemistry

Tumor tissue sections extracted from MMTV-PyMT mice were fixed with 4% (v/v) paraformaldehyde in PBS for 10 min at room temperature. After incubating with primary antibodies overnight at 4°C, endogenous peroxidases in the samples were oxidized by exposure to 0.3% H_2O_2 in TBS for 15 min at room temperature. Samples were then incubated with secondary antibody, horseradish peroxidase–conjugated anti-rabbit goat antibody (611-103-122, Rockland Immunochemicals, Limerick, PA, USA) at 1:400 diluted in TBS with 10% (v/v) FBS and 10% goat serum for 1 hour at room temperature. Samples were then incubated with 3,3'-Diaminobenzidine (DAB) (Cell Signaling Technology) for signal development and with Mayer's hematoxylin for counterstaining. After dehydration and mounting, tissue sections were then digitalized using the Leica SCN400 Slide Scanner. Signal intensity and percentage of the signal-positive area were quantified with Leica Digital Image Hub.

Comet assay

The comet assay was performed according to the protocol described previously (*19*). MET-1 cells treated with STZ for 5 days were suspended in 1% low gelling temperature agarose (Sigma-Aldrich; type VII, catalog no. A-4018) in PBS at 37°C and pipetted immediately onto a glass slide with a layer of 1% agarose. After agarose has gelled, slides were first immersed in alkaline lysis solution at 4°C overnight and then rinsed at room temperature for 20 min. After three rinses, slides were transferred into an electrophoresis tank and undergo electrophoresis for 20 min at a voltage of 0.6 V/cm. After electrophoresis, slides were rinsed in distilled water and stained with propidium iodide at 2.5 μg/ml concentration in distilled water for 20 min. Slides were then rinsed and imaged with a Zeiss LSM700 confocal microscope using a 20×/1.1 NA water immersion objective and *z*-stack imaging. The tail moment, which represents DNA damage, was quantified using Comet Assay IV software (Instem, Staffordshire, UK).

TUNEL assay

The TUNEL assay was performed using a Click-iT Plus TUNEL Assay kit (C10617, Thermo Fisher Scientific) and per the instruction provided by the manufacturer.

Deoxyribonuclease-treated cells were included as a positive control for the assay. Slides were imaged using with a Zeiss LSM700 confocal microscope using a 20×/1.1 NA water immersion objective and *z*-stack imaging.

Collagen deposition assay

Fixed tumor sections collected from PyMT mice were hydrated and stained using a Picrosirius red stain kit (24901-250, Polysciences Inc.) according to the manufacturer's instructions. After dehydration and mounting, quantitative polarization microscopy was performed on the sections as previously described using an inverted Axiovert microscope equipped with a rotatable linear polarizer and a circular polarizer with a Zeiss Axiocam 506 color camera (*52*). Quantification of optical retardance was performed using the preestablished method (*52*). Briefly, average retardance of a randomly selected region of interest from each image with background subtraction was used to quantify collagen content in the tumor sections.

Unconfined compression assay

Snap-frozen tumors from PyMT mice were thawed in PBS with protease inhibitor cocktail immediately before mechanical testing was performed as described previously (*21*). Tumor mechanical properties were measured using a TA Electroforce Model 3100 (TA Instruments). Tissues were subjected to 15% strain with 3% stepwise displacements over five steps. Each step consisted of a 1-mm indentation with a 15-min relaxation time. Using a custom MATLAB script, the equilibrium modulus was calculated from the slope of the stress-strain curves generated using a poroviscoelastic model.

Analysis of human breast tumor

To examine the correlation between glycation and tumor progression, tumor specimens from diabetic or nondiabetic breast cancer patients were obtained from Cooperative Human Tissue Network according to the protocol approved by the Institutional Review Board (IRB) at the Vanderbilt University Medical Center (IRB no. 201314, see corresponding clinical information in table S1). Snap-frozen breast tumors were obtained and sectioned at a thickness of 8 μm for immunofluorescence staining and immunochemistry staining or at 20 μm for AFM.

Statistical analysis

Statistical analysis was performed with GraphPad Prism 8.0a (GraphPad Software, La Jolla, CA, USA). Data here are presented as means ± SEM. Two tailed *t* test was used for comparisons of two groups. When more than two groups were analyzed, parametric one- or two-tailed one-way analysis of variance (ANOVA) followed by a Mann-Whitney test or a post hoc Tukey's test were used where appropriate. $P < 0.05$ was considered statistically significant.

SUPPLEMENTARY MATERIALS

Supplementary material for this article is available at https://science.org/doi/10.1126/sciadv.abo1673

View/request a protocol for this paper from *Bio-protocol*.

REFERENCES AND NOTES

1. M. Abudawood, Diabetes and cancer: A comprehensive review. *J. Res. Med. Sci.* **24**, 94 (2019).
2. S. L. Habib, M. Rojna, Diabetes and risk of cancer. *ISRN Oncol.* **2013**, 583786 (2013).
3. E. Giovannucci, D. M. Harlan, M. C. Archer, R. M. Bergenstal, S. M. Gapstur, L. A. Habel, M. Pollak, J. G. Regensteiner, D. Yee, Diabetes and cancer: A consensus report. *Diabetes Care* **33**, 1674–1685 (2010).
4. T. Y. Ryu, J. Park, P. E. Scherer, Hyperglycemia as a risk factor for cancer progression. *Diabetes Metab. J.* **38**, 330–336 (2014).
5. K. Ozer, M. O. Horsanali, S. N. Gorgel, E. Ozbek, Diabetes is an important risk factor for metastasis in non-muscle-invasive bladder cancer. *Asian Pac. J. Cancer Prev.* **17**, 105–108 (2016).
6. Y. R. Li, V. Ro, J. C. Tchou, Obesity, metabolic syndrome, and breast cancer: From prevention to intervention. *Curr. Surg. Rep.* **6**, 7 (2018).
7. B. N. Mason, A. Starchenko, R. M. Williams, L. J. Bonassar, C. A. Reinhart-King, Tuning three-dimensional collagen matrix stiffness independently of collagen concentration modulates endothelial cell behavior. *Acta Biomater.* **9**, 4635–4644 (2013).
8. B. N. Mason, C. A. Reinhart-King, Controlling the mechanical properties of three-dimensional matrices via non-enzymatic collagen glycation. *Organogenesis* **9**, 70–75 (2013).
9. J. G. Snedeker, A. Gautieri, The role of collagen crosslinks in ageing and diabetes–The good, the bad, and the ugly. *Muscles, Ligaments Tendons J.* **4**, 303–308 (2014).
10. N. W. Seidler, C. Kowalewski, Methylglyoxal-induced glycation affects protein topography. *Arch. Biochem. Biophys.* **410**, 149–154 (2003).
11. H. Xing, V. Yaylayan, Mechanochemically induced controlled glycation of lysozyme and its effect on enzymatic activity and conformational changes. *J. Agric. Food Chem.* **67**, 3249–3255 (2019).
12. M. Brownlee, A. Cerami, H. Vlassara, Advanced glycosylation end products in tissue and the biochemical basis of diabetic complications. *N. Engl. J. Med.* **318**, 1315–1321 (1988).
13. V. P. Singh, A. Bali, N. Singh, A. S. Jaggi, Advanced glycation end products and diabetic complications. *Korean J. Physiol. Pharmacol.* **18**, 1–14 (2014).
14. J. L. Leight, M. A. Wozniak, S. Chen, M. L. Lynch, C. S. Chen, Matrix rigidity regulates a switch between TGF-β1–induced apoptosis and epithelial–mesenchymal transition. *Mol. Biol. Cell* **23**, 781–791 (2012).
15. A. Pathak, S. Kumar, Transforming potential and matrix stiffness co-regulate confinement sensitivity of tumor cell migration. *Integr. Biol. (Camb.)* **5**, 1067–1075 (2013).
16. C. Cojocel, L. Novotny, A. Vachalkova, B. Knauf, Comparison of the carcinogenic potential of streptozotocin by polarography and alkaline elution. *Neoplasma* **50**, 110–116 (2003).
17. A. D. Bolzán, M. S. Bianchi, Genotoxicity of streptozotocin. *Mutat. Res. Rev. Mutat. Res.* **512**, 121–134 (2002).
18. R. N. Arison, E. L. Feudale, Induction of renal tumour by streptozotocin in rats. *Nature* **214**, 1254–1255 (1967).
19. P. L. Olive, J. P. Banáth, The comet assay: A method to measure DNA damage in individual cells. *Nat. Protoc.* **1**, 23–29 (2006).
20. A. D. Borowsky, R. Namba, L. J. T. Young, K. W. Hunter, J. G. Hodgson, C. G. Tepper, E. T. McGoldrick, W. J. Muller, R. D. Cardiff, J. P. Gregg, Syngeneic mouse mammary carcinoma cell lines: Two closely related cell lines with divergent metastatic behavior. *Clin. Exp. Metastasis* **22**, 47–59 (2005).

21. F. Bordeleau, B. N. Mason, E. M. Lollis, M. Mazzola, M. R. Zanotelli, S. Somasegar, J. P. Califano, C. Montague, D. J. LaValley, J. Huynh, N. Mencia-Trinchant, Y. L. Negron Abril, D. C. Hassane, L. J. Bonassar, J. T. Butcher, R. S. Weiss, C. A. Reinhart-King, Matrix stiffening promotes a tumor vasculature phenotype. *Proc. Natl. Acad. Sci. U.S.A.* **114**, 492–497 (2017).
22. M. J. Paszek, N. Zahir, K. R. Johnson, J. N. Lakins, G. I. Rozenberg, A. Gefen, C. A. Reinhart-King, S. S. Margulies, M. Dembo, D. Boettiger, D. A. Hammer, V. M. Weaver, Tensional homeostasis and the malignant phenotype. *Cancer Cell* **8**, 241–254 (2005).
23. S. C. Wei, L. Fattet, J. H. Tsai, Y. Guo, V. H. Pai, H. E. Majeski, A. C. Chen, R. L. Sah, S. S. Taylor, A. J. Engler, J. Yang, Matrix stiffness drives epithelial-mesenchymal transition and tumour metastasis through a TWIST1-G3BP2 mechanotransduction pathway. *Nat. Cell Biol.* **17**, 678–688 (2015).
24. J. Park, J. E. Schwarzbauer, Mammary epithelial cell interactions with fibronectin stimulate epithelial-mesenchymal transition. *Oncogene* **33**, 1649–1657 (2014).
25. J. K. Slack-Davis, K. H. Martin, R. W. Tilghman, M. Iwanicki, E. J. Ung, C. Autry, M. J. Luzzio, B. Cooper, J. C. Kath, W. G. Roberts, J. T. Parsons, Cellular characterization of a novel focal adhesion kinase inhibitor. *J. Biol. Chem.* **282**, 14845–14852 (2007).
26. I. Pastushenko, C. Blanpain, EMT transition states during tumor progression and metastasis. *Trends Cell Biol.* **29**, 212–226 (2019).
27. H. Ou, Y. Huang, L. Xiang, Z. Chen, Y. Fang, Y. Lin, Z. Cui, S. Yu, X. Li, D. Yang, Circulating tumor cell phenotype indicates poor survival and recurrence after surgery for hepatocellular carcinoma. *Dig. Dis. Sci.* **63**, 2373–2380 (2018).
28. H. Polioudaki, S. Agelaki, R. Chiotaki, E. Politaki, D. Mavroudis, A. Matikas, V. Georgoulias, P. A. Theodoropoulos, Variable expression levels of keratin and vimentin reveal differential EMT status of circulating tumor cells and correlation with clinical characteristics and outcome of patients with metastatic breast cancer. *BMC Cancer* **15**, 399 (2015).
29. M. Heron, Deaths: Leading causes for 2017. *Natl. Vital Stat. Rep.* **68**, 1–77 (2019).
30. T. Jensen, T. Deckert, Diabetic retinopathy, nephropathy and neuropathy. Generalized vascular damage in insulin-dependent diabetic patients. *Horm. Metab. Res. Suppl.* **26**, 68–70 (1992).
31. M. W. Nasser, N. A. Wani, D. K. Ahirwar, C. A. Powell, J. Ravi, M. Elbaz, H. Zhao, L. Padilla, X. Zhang, K. Shilo, M. Ostrowski, C. Shapiro, W. E. Carson III, R. K. Ganju, RAGE mediates S100A7-induced breast cancer growth and metastasis by modulating the tumor microenvironment. *Cancer Res.* **75**, 974–985 (2015).
32. T. Kwak, K. Drews-Elger, A. Ergonul, P. C. Miller, A. Braley, G. H. Hwang, D. Zhao, A. Besser, Y. Yamamoto, H. Yamamoto, D. El-Ashry, J. M. Slingerland, M. E. Lippman, B. I. Hudson, Targeting of RAGE-ligand signaling impairs breast cancer cell invasion and metastasis. *Oncogene* **36**, 1559–1572 (2017).
33. D. R. Sell, J. F. Nelson, V. M. Monnier, Effect of chronic aminoguanidine treatment on age-related glycation, glycoxidation, and collagen cross-linking in the Fischer 344 rat. *J. Gerontol. A Biol. Sci. Med. Sci.* **56**, B405–B411 (2001).
34. M. T. Coughlan, J. M. Forbes, M. E. Cooper, Role of the AGE crosslink breaker, alagebrium, as a renoprotective agent in diabetes. *Kidney Int.* **72**, S54–S60 (2007).
35. R. Rak, R. Haklai, G. Elad-Tzfadia, H. J. Wolfson, S. Carmeli, Y. Kloog, Novel LIMK2 inhibitor blocks Panc-1 tumor growth in a mouse xenograft model. *Onco. Targets. Ther.* **1**, 39–48 (2014).
36. S. Nam, V. K. Gupta, H.-p. Lee, J. Y. Lee, K. M. Wisdom, S. Varma, E. M. Flaum, C. Davis, R. B. West, O. Chaudhuri, Cell cycle progression in confining microenvironments is regulated by a growth-responsive TRPV4-PI3K/Akt-p27Kip1 signaling axis. *Sci. Adv.* **5**, eaaw6171 (2019).
37. C. Prasad, K. E. Davis, V. Imrhan, S. Juma, P. Vijayagopal, Advanced glycation end products and risks for chronic diseases: Intervening through lifestyle modification. *Am. J. Lifestyle Med.* **13**, 384–404 (2019).
38. H. Younus, S. Anwar, Prevention of non-enzymatic glycosylation (glycation): Implication in the treatment of diabetic complication. *Int. J. Health Sci. (Qassim)* **10**, 261–277 (2016).
39. A. Nenna, F. Nappi, S. S. Avtaar Singh, F. W. Sutherland, F. Di Domenico, M. Chello, C. Spadaccio, Pharmacologic approaches against advanced glycation end products (AGEs) in diabetic cardiovascular disease. *Res. Cardiovasc. Med.* **4**, e26949 (2015).
40. X.-B. Zhao, G.-S. Ren, Diabetes mellitus and prognosis in women with breast cancer: A systematic review and meta-analysis. *Medicine (Baltimore)* **95**, e5602 (2016).
41. S. W. Lahiri, Management of type 2 diabetes: What is the next step after metformin? *Clin. Diabetes* **30**, 72–75 (2012).
42. P. Saraei, I. Asadi, M. A. Kakar, N. Moradi-Kor, The beneficial effects of metformin on cancer prevention and therapy: A comprehensive review of recent advances. *Cancer Manag. Res.* **11**, 3295–3313 (2019).
43. M. Li, J. Cao, Y. He, Z. Zhou, X. He, Q.-Q. Zhang, L.-J. Wang, C.-L. Qi, Generation and biological characteristics of a mouse model of breast cancer that copresents with diabetes mellitus. *Anat. Rec. (Hoboken)* **302**, 269–277 (2019).
44. A. Faustino-Rocha, P. A. Oliveira, J. Pinho-Oliveira, C. Teixeira-Guedes, R. Soares-Maia, R. G. da Costa, B. Colaco, M. J. Pires, J. Colaco, R. Ferreira, M. Ginja, Estimation of rat mammary tumor volume using caliper and ultrasonography measurements. *Lab Anim. (NY)* **42**, 217–224 (2013).
45. Z. Maria, A. R. Campolo, B. J. Scherlag, J. W. Ritchey, V. A. Lacombe, Insulin treatment reduces susceptibility to atrial fibrillation in Type 1 diabetic mice. *Front. Cardiovasc. Med.* **7**, 134 (2020).
46. R. C. Ransom, A. C. Carter, A. Salhotra, T. Leavitt, O. Marecic, M. P. Murphy, M. L. Lopez, Y. Wei, C. D. Marshall, E. Z. Shen, R. E. Jones, A. Sharir, O. D. Klein, C. K. F. Chan, D. C. Wan, H. Y. Chang, M. T. Longaker, Mechanoresponsive stem cells acquire neural crest fate in jaw regeneration. *Nature* **563**, 514–521 (2018).
47. A. Saadane, E. M. Lessieur, Y. Du, H. Liu, T. S. Kern, Successful induction of diabetes in mice demonstrates no gender difference in development of early diabetic retinopathy. *PLOS ONE* **15**, e0238727 (2020).
48. K. Nonogaki, A. M. Strack, M. F. Dallman, L. H. Tecott, Leptin-independent hyperphagia and type 2 diabetes in mice with a mutated serotonin 5-HT_{2C} receptor gene. *Nat. Med.* **4**, 1152–1156 (1998).
49. B. L. Furman, Streptozotocin-induced diabetic models in mice and rats. *Curr. Protoc. Pharmacol.* **70**, 5.47.41–5.47.20 (2015).
50. B. S. Nielsen, M. Egeblad, F. Rank, H. A. Askautrud, C. J. Pennington, T. X. Pedersen, I. J. Christensen, D. R. Edwards, Z. Werb, L. R. Lund, Matrix metalloproteinase 13 is induced in fibroblasts in polyomavirus middle T antigen-driven mammary carcinoma without influencing tumor progression. *PLOS ONE* **3**, e2959 (2008).
51. J. Huynh, N. Nishimura, K. Rana, J. M. Peloquin, J. P. Califano, C. R. Montague, M. R. King, C. B. Schaffer, C. A. Reinhart-King, Age-related intimal stiffening enhances endothelial permeability and leukocyte transmigration. *Sci. Transl. Med.* **3**, 112ra122 (2011).
52. W. Wang, E. M. Lollis, F. Bordeleau, C. A. Reinhart-King, Matrix stiffness regulates vascular integrity through focal adhesion kinase activity. *FASEB J.* **33**, 1199–1208 (2019).

Acknowledgments: We appreciate A. Borowsky for providing the MET-1 cell line. This work was performed in part at the Translational Pathology Shared Resource at the Vanderbilt University Medical Center (VUMC), which is supported by NCI/NIH Cancer Center Support Grant 2P30 CA068485-14 and the Vanderbilt Mouse Metabolic Phenotyping Center Grant 5U24DK059637-13. Whole slide imaging and quantification of immunostaining were performed in the Digital Histology Shared Resource at VUMC (www.vumc.org/dhsr/welcome). **Funding:** This work was supported by the Keck Foundation, the NIH (GM131178 and HL127499) to C.A.R.-K.; an AHA Predoctoral Fellowship (917613) and a Predoctoral to Postdoctoral Fellow Transition Award (1F99CA274695-01) to W.W.; an F31 Predoctoral Individual National Research Service Award (under grant no. 1F31HL154727) to P.V.T.; T32 Fellowship Award (under grant no. DK101003) to trainees K.S. and L.G.; and National Science Foundation Graduate Research Fellowship Award (under grant no. DGE-1650441) to L.A.H. This work was supported in part by NIH grants P30-DK114809 and R01-DK119212 to A.P. and by the Department of Veterans Affairs Merit Reviews 1I01BX002025 to A.P. A.P. is the recipient of a Department of Veterans Affairs Senior Research Career Scientist Award. **Author contributions:** W.W., L.A.H., L.G., A.P., N.J.F., and C.A.R.-K. designed research; W.W., L.A.H., L.G., Y.W., K.S., M.M.R., K.M.Y., M.E.B., and A.C.J. performed the experiments; W.W., L.A.H., Y.W., and P.V.T. analyzed data; C.A.R.-K. supervised the study. W.W., L.A.H., and C.A.R.-K. wrote and edited the manuscript. A.P. edited the manuscript. **Competing interests:** The authors declare that they have no competing interests. **Data and materials availability:** All data needed to evaluate the conclusions in the paper are present in the paper and/or the Supplementary Materials.

Submitted 18 January 2022
Accepted 29 September 2022
Published 18 November 2022
10.1126/sciadv.abo1673